Revision of capillary cone-jet physics: Electrospray and flow focusing

Alfonso M. Gañán-Calvo

Departamento de Ingeniería Aeroespacial y Mecánica de Fluidos, Universidad de Sevilla, E-41092 Sevilla, Spain

José M. Montanero

Departamento de Ingeniería Mecánica, Energética y de los Materiales, Universidad de Extremadura, E-06071 Badajoz, Spain

Capillary cone jets are natural microfluidic structures arising in steady capillary tip streaming, whose paradigms are electrospray and flow focusing phenomena. In this work, we make a profound revision of the basic underlying physics of generic cone jets from thousands of experimental measurements, most of them reported in the literature. First, the boundaries of the stability region of steady jetting are calculated. We describe these limitations by instability mechanisms associated with the local flow structure in the tip and the issuing jet and with the global behavior of the meniscus. Second, to undertake a general physical treatment of cone jets in steady regime, we analyze the energy balance taking place in the tips of both flow focusing and electrospray. This analysis yields a fundamental result: if the electrospray data are expressed in terms of an effective pressure drop, both phenomena satisfy the same scaling law for the droplet size, which exhibits nearly complete similarity in the parameter window where quasimonodisperse sprays are produced. That effective pressure drop is a function of the liquid properties exclusively, i.e., it does not depend on the operational parameters (flow rate and applied voltage). Moreover, the stability limits of the operational regimes are analyzed in detail, finding fundamental coincidences between flow focusing and electrospray as well. These results provide most useful general description and predictive scaling laws for nearly monodisperse microspraying or nanospraying based on steady cone jets, of immediate applicability in analytical chemistry, chemical engineering, biochemistry, pharmaceutical and food technologies, painting, and many other technological fields.

I. INTRODUCTION

Different techniques have been proposed to generate capillary microjets.[1] Here, we focus on tapering microjets or cone jets. Phenomena giving rise to these peculiar local structures are often referred to as realizations of "tip streaming." Tip streaming is used to produce small droplets and bubbles under a great variety of conditions. Here, we distinguish unsteady from steady tip streaming. While unsteady tip streaming (UTS) plays an essential role in drop-on-demand applications, steady tip streaming (STS) is of fundamental importance in the mass and long-term production of droplets and bubbles with a precisely controlled size. UTS driven by either hydrodynamic [1] or electrohydrodynamic [2,3] means has recently been analyzed using full numerical simulations [2,4]. These studies revealed fundamental differences between UTS and STS driven by electrohydrodynamic forces, in contrast to prior assumptions [5,6], and provided a highly detailed scrutiny of the transient formation of an electrohydrodynamically driven spout [2].

In UTS, charge relaxation phenomena cause intense electric fields in the liquid and consequently induce large transient shear stresses and polarization forces, which cannot be predicted from simple estimations and comparisons between the relaxation of charges, flow times, or the duration of emissions. If the system possesses an attractor corresponding to a steady state for the operational parameters considered, then those forces decay in times usually comparable to the residence time of the liquid in the meniscus (not in the jet). Once the steady regime is reached, convective inertia and capillary and viscous forces balance the external forces imposed by pressure gradients, electric or chemical potentials, etc. In STS, local acceleration and other transient effects (including polarization forces) decay in times comparable to the flow evolution in the meniscus when the system selects its steady attractor. The internal electric field is limited by Ohmic conduction due to the global charge conservation constraint, and therefore charge relaxation on the free surface is not a determining factor. Indeed, the scaling laws and asymptotic features describing the transient regimes [2,4] differ significantly from those for the corresponding steady states [7]. Thus, the introduction of concepts like the (intrinsically unsteady) charge "rarefaction fronts" [6] to justify assumptions made for STS [8] cannot support the suggested scalings [8] but emphasize inconsistencies subsequently found, as discussed in this paper.

In the present work, we focus on the STS phenomenon for its interest in the massive continuous production of high quality sprays. Several atomization regimes have been found in the realizations of STS. In the steady jetting regime, a long jet extends downstream and then breaks into droplets through Rayleigh instability [9,10]. Steady jetting gives rise to great productivity and well-controlled drop size. Therefore, it is of interest and importance to understand and quantitatively describe what are the mechanisms of instability that may prevent the steady jetting regime being reached in the realizations of STS. Cone-jet electrospray (ES) and flow focusing (FF) are two examples of STS phenomena. These atomization techniques working in the steady jetting regime utilize locally available differences of energies to produce a capillary jet. A voltage difference between the liquid and an

---

[1]For details of the proposals, see Ref. [68].

external electrode is applied to move the liquid in ES, while in FF the energy source is the pressure drop applied to the focusing gas, which is forced through an orifice. A large number of ES and FF experiments have been conducted and reported in the literature to map the parameter regions where steady jetting is obtained and to show the size of the resulting droplets.

In general, steady jetting requires a cusplike or peak-ended liquid meniscus from whose tip tapers a steady jet. The meniscus may globally be either stable or unstable depending on the values of the operational parameters. The global stability of the liquid meniscus is a prerequisite for steady jetting. In addition, the jet issued by the meniscus may be either convectively or absolutely unstable depending on its radius, velocity profile, and liquid properties (see, e.g., [11–14]). Convective instability occurs when a localized initial distortion travels downstream in the fluid domain, preserving a stable liquid ligament close to the meniscus. On the contrary, the jet is absolutely unstable if the distortion spreads in both downstream and upstream directions, preventing the formation of the liquid ligament. Therefore, the convective instability of the jet is an additional condition for steady jetting.

Local absolute instability does not necessarily cause global instability. Perturbations in absolutely unstable jets may grow and cause breakup very shortly downstream of the neck. This situation occurs when the maximum growth rate of the perturbations is significantly greater than that of the front moving upstream [15]. In this case, the propagation medium (the free surface) pinches off and disrupts periodically, preventing the propagation upstream of growing waves. This phenomenon was observed in microbubbling experiments [16,17] and confirmed by numerical simulations [18]. In both cases, the bubble size was determined by the Rayleigh instability of the jet periodically formed in an early stage [9]. Transitions from convective to absolute instability may take place downstream due to momentum diffusion and flow divergence in the external coflow speed [19], leading to the formation of large drops in the transition region. We will not consider this case because it is not applicable to ES and has not been observed in FF for practical gas speeds.

To summarize, we will here consider as steady jetting that regime where (i) the liquid meniscus is globally stable, (ii) the emitted jet is convectively unstable, so that a stable liquid ligament with an axial length long compared to its diameter can be found behind the neck, and (iii) the resulting droplets are commensurate with the jet diameter due to Rayleigh instability [9,10].

The interesting work by Marginean *et al.* [20] provides a coherent picture of the ES regimes, describing the place occupied by STS-ES (or cone-jet ES) in the broader context of ES regimes [21]. Cone-jet ES has been the subject of many experimental and theoretical studies going back to Zeleny [22]. Hayati *et al.* [23], Cloupeau and Prunet-Foch [24], Fernandez de la Mora and co-workers [6,8,25], Hartman *et al.* [26], and Higuera [27], among many others, have continuously provided results over the last decades. In particular, the works by Fernandez de la Mora and Loscertales [8,28] rank among the first partially successful rationalizations to reduce cone-jet ES to workable models and simple predictive

scaling laws on the basis of dimensional analysis. However, the role played by the liquid polarity and the behavior of ionic species in the liquid was not satisfactorily described, as subsequent studies have revealed [26,29–31]. These issues still stir controversy [1,2,6,7] and require clarification.

Much effort has been devoted to the theoretical analysis of ES in the last few decades. A semi-infinite electrostatic conical solution was found by Taylor [32] for an electrified meniscus at equilibrium. The absence of an electric potential difference as a parameter of the solution aroused a certain doubt about its validity for real problems. Taylor's solution was incorporated in a problem with realistic boundary conditions (a finite size capillary needle, a counterelectrode, etc.) in [33]. The controversy was resolved by identifying an eigenvalue for a real capillary-meniscus-electrode configuration: the applied voltage necessary to get an equilibrium solution with a conical apex for a given meniscus volume or alternatively for a given pressure in the meniscus. The relevance of Taylor's solution for a real problem was finally demonstrated since it was the necessary asymptotic local solution at the tip of the meniscus to support the existence of a conical peak.

Taylor's peak-ended solution provides a fundamental support ("framework") to sustain the existence of tapering menisci in ES. On the contrary, there is no solution of comparable universality and validity in STS driven by mechanical energy (e.g., FF). In this context, Zhang [34] found families of solutions for creeping flows in the limit of vanishing issued flow rate. However, although there has been speculation about the existence of solutions for more general situations (see, e.g., [35]), they have never been found. In the absence of such solutions, one can make use of *de facto* physical reasoning and dimensional analysis tools.

The electrostatic solutions for ES require a vanishing radius of curvature at the tip, which yields a diverging electric field, among other singularities, at that point. For this reason, the stability of the meniscus is linked to the emission of a liquid flow rate above a *finite* critical value Q_{min} which depends mainly on the liquid properties. Below Q_{min}, the meniscus is unstable for any applied voltage and oscillates with varying frequencies. Above Q_{min}, there is a relatively narrow range of applied voltage for which the system exhibits steady jetting (see, e.g., [30,36]). Within this range, the volume of the tapering meniscus is a function of the applied voltage in good agreement with the equilibrium solution found in [33]. When the meniscus volume is below (above) its equilibrium value, the issued flow rate should be smaller (greater) than the incoming flow rate from the feeding capillary. The difference between the two flow rates should go to zero with time as the meniscus volume approaches its eventual equilibrium value. If this self-adjustment does not take place for the imposed flow rate and voltage, the experimenter should adjust one of those parameters until stability is reached. This well-known operation reflects the intrinsic dependence of the operational parameter ranges on the liquid properties for ES liquid atomization. In contrast, the pressure drop applied in FF can be chosen by the experimenter practically at will, and the issued liquid flow rate is almost independent of that quantity. In FF, the lower limit Q_{min} of the issued flow rate for steady jetting is generally a function of the applied pres-

sure drop. It must be noted that Q_{min} can reach much smaller values in FF than in ES for many moderately low conductivity solvents since in ES the smaller the electrical conductivity the larger Q_{min} [7,37]. Indeed, FF is a viable alternative scheme to produce submicron and nanometer jets [38], in contrast to that claimed in [6] (page 219).

In spite of the differences between ES and FF described above, there are intriguing common features that deserve investigation. Indeed, these analogies were the serendipitous motto for the discovery of FF in 1994 [39] during an investigation on ES and have led to the successful combination of FF and ES [40]. The most important analogies in the steady jetting regime are the following: (i) both ES and FF exhibit static menisci (fluid regions held by surface tension) with more or less pronounced conelike or tapering shapes; (ii) the apparent similarity between the tapering regions of the two types of meniscus; and (iii) the disparity between the size of that region and the dimensions of the experimental device (feeding capillary and the exit orifice in FF). These common features have inspired previous attempts to describe ES and FF in terms of a universal self-similar flow structure in the tapering region. A possible unification of the two problems has been proposed based on the analysis of the momentum equation for the issuing jet [40].

In this work, we focus on liquid cone jets surrounded by a gas or vacuum since the liquid-liquid case does not add additional physical ingredients and is significantly simpler in most cases (the two liquids move with nearly the same velocity). We aim to inquire into the physical parallelism between ES and gas-assisted FF. We explore an argument based on the energy balance that takes place in the tip region of both ES and FF which will unveil additional analogies and resemblances, showing the common roots of ES and FF as STS phenomena. We also analyze the differences between the flow structure in the liquid meniscus of ES and FF, which yield significant discrepancies between the stabilities of the steady regime in both cases. Our study will be validated by experiments conducted in the present work and mainly by the experimental data collected from an extensive literature review.

The organization of the paper is as follows. A unified description of STS in ES and FF is proposed in Sec. II. The experimental validation of our predictions for the stability limits of the steady jetting regime is presented in Sec. III. In Sec. IV, we describe the effects of the tangential viscous stress exerted by the gas and the recirculation pattern in the meniscus of FF. The scaling law for the resulting droplet radius in both ES and FF is studied in Sec. V. The paper closes with some conclusions in Sec. VI.

II. ENERGY ANALYSIS: A UNIFIED PHYSICAL DESCRIPTION

A. Formulation of the ES and FF problems

In STS, a flow rate Q is emitted through a jet tapering from the apex of a cusplike axisymmetric liquid meniscus of density ρ and viscosity μ. The meniscus is held by the surface tension σ between the liquid and the environment, air in most cases. In general, the jet radius depends on the distance
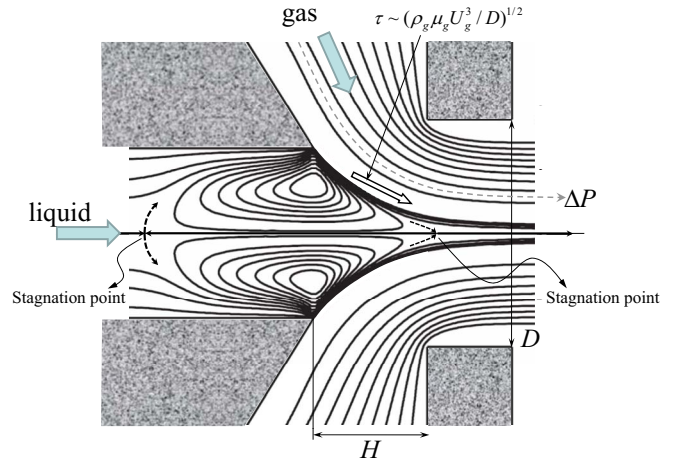

FIG. 1. (Color online) Typical flow pattern in FF. Streamlines of the liquid and gas phases [43].

from the meniscus. However, it reaches an almost uniform value R downstream in the proximity of the breakup region. The dimensionless Weber, Reynolds, and capillary numbers characterizing the jet's behavior can be defined from the above quantities as

$$\text{We} = \frac{\rho Q^2}{\pi^2 R^3 \sigma}, \quad \text{Re} = \frac{\rho Q}{\pi R \mu}, \quad \text{Ca} = \frac{\text{We}}{\text{Re}}. \quad (1)$$

The diameter of the feeding capillary is much larger than that of the issuing jet, and thus it does not affect the energy balance at the tip. For this reason, it will not be considered in this section. Thermal effects, such as the Marangoni convection, are of negligible importance in most realizations of STS, and thus they will not be taken into account in the present work.

Figure 1 shows the FF configuration. The energy source is the pressure drop ΔP applied to the focusing gas, which is forced through an orifice. In most cases, the gas flow can be considered as incompressible and inviscid. One assumes that both the liquid and the gas come from reservoirs kept at the same pressure. As in ES, the size of the neck-jet region is much smaller than the dimensions characterizing the FF geometry (the diameters of the orifice and the capillary and the capillary-orifice distance). For this reason, these dimensions are not considered in this section.

Figure 2 shows the cone-jet configuration appearing in ES. Magnetic effects are negligible in ES, and thus only mechanical and electrical aspects are considered. A voltage difference V is applied between the liquid and an external electrode. The bulk free charges move to the free surface, where the resulting electric field leads to the appearance of Maxwell stresses proportional to the permittivity of vacuum ε_0. The meniscus reaches a conical shape as the result of the balance between the pressure jump across the free surface, the surface tension, and the Maxwell stresses. Charge is both convected and conducted by the liquid jet. The conduction can be described by the Ohmic model, K being the electrical conductivity. Because the energy dissipated by the charge transport (Joule effect) through the bulk is smaller than or at most comparable to the liquid kinetic energy [27,40,41], de-
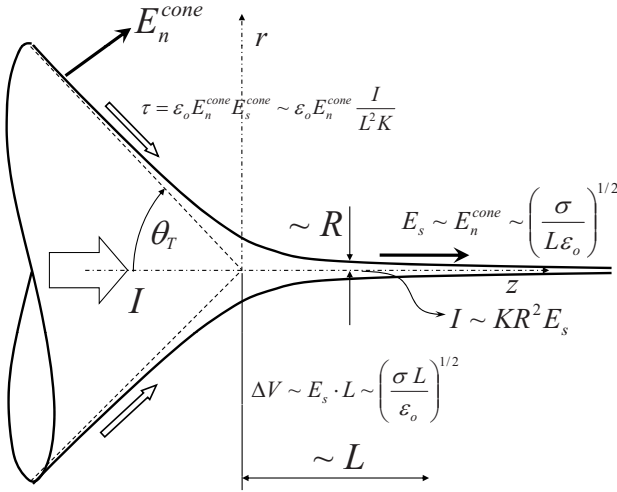
FIG. 2. Sketch of the Taylor cone-jet region. The solid angle θ_T represents the underlying Taylor's conical solution. The rest of the quantities are defined in the main text.

tails of the electrical conduction are not required for the purposes of our analysis.

To summarize, the liquid properties $\{\rho, \mu, \sigma\}$ are involved in our energy analysis of both ES and FF, while the electrical quantities $\{K, \varepsilon_0\}$ enter in ES only. The flow rate Q is one of the two operational parameters in both phenomena. The others are the voltage V in ES and the pressure ΔP in FF.

B. Energy balance in FF

The energy dissipated by viscosity in the steady jetting regime of FF is negligible for the operating ranges of interest in this study. To demonstrate this assertion, let us consider the Reynolds number $\text{Re}_g = \rho_g U_g D / \mu_g$ of the gas flow through the orifice, where ρ_g, μ_g, and U_g are the density, viscosity, and typical velocity of the gas forced through the orifice of diameter D, respectively. Because Re_g takes large numbers (on the order of $10^2 - 10^5$), $U_g \sim (\Delta P / \rho_g)^{1/2}$ and the viscous effects are confined to thin accelerated boundary layers at the orifice walls and the meniscus surface. These boundary layers have a thickness $\delta \sim D / \text{Re}_g^{1/2}$, assuming that the velocity in the liquid meniscus is very small compared with that of the gas. The tangential viscous stress τ_s exerted by the gas flow on the meniscus surface can be estimated as

$$\tau_s \sim \mu_g U_g / \delta \sim (\rho_g \mu_g U_g^3 D^{-1})^{1/2} \sim (\mu_g \rho_g^{-1/2} \Delta P^{3/2} D^{-1})^{1/2}. \tag{2}$$

The surface tension stress $\tau_\sigma \sim \sigma / D$ is small compared with the total pressure drop ΔP applied on both the gas and the liquid. The comparison between ΔP and τ_s yields [42]

$$\tau_s / \Delta P \sim \left(\frac{\mu_g}{D \rho_g^{1/2} \Delta P^{1/2}} \right)^{1/2} = \text{Re}_g^{-1/2}, \tag{3}$$

which justifies that the accelerating effect of τ_s on the liquid can be neglected once the steady jetting regime has been established. It must be noted that this does not imply that τ_s can be neglected in FF. As will be shown in Sec. IV, τ_s plays

a crucial role at the initial stages of FF when the steady jetting regime is establishing.

In summary, one can assert that, in the steady jetting regime and for the operating ranges of interest in this study, the energy applied onto the liquid per unit time, $\Delta P Q$, is mainly invested in generating kinetic energy, $\rho U^2 Q$, where U is the characteristic jet velocity. Therefore,

$$\left. \begin{array}{c} \Delta P \cdot Q \sim \rho U^2 Q \\ U \sim Q/R^2 \end{array} \right\} \Rightarrow \begin{cases} R \sim \left(\dfrac{\rho Q^2}{\Delta P} \right)^{1/4} \\ U \sim (\Delta P/\rho)^{1/2}. \end{cases} \tag{4}$$

These scalings can also be obtained from an analysis of the momentum balance [39]. As was anticipated above, the jet radius R is mainly independent of the geometrical dimensions characterizing the FF configuration. One can estimate R from the exact balance between applied pressure and resulting kinetic energy, which yields [39]

$$R = \left(\frac{\rho Q^2}{2\pi^2 \Delta P} \right)^{1/4}. \tag{5}$$

Equation (5) is in remarkable agreement with experiments, as reported by numerous studies going back to 1998 (see [17,39,43–45]).

Because the free surface and internal energy sinks (viscous dissipation) are of secondary importance in most practical conditions, they are not considered in this first approach. However, the kinetic energy may become comparable to that associated with the free surface or that dissipated by viscosity as the flow rate Q decreases and approaches the stability limit. In this case, σ and μ enter the energy balance. For sufficiently small values of Q, surface tension consumes a significant part of the applied energy when the jet is emitted. This loss of kinetic energy may halt the emission. When the emission is halted, the free surface energy sink disappears because the meniscus tip becomes blunt. Then, the meniscus slowly inflates until a portion of its tip becomes drawn into the orifice and ejected as an unsteady spitting. In this situation, the flow becomes globally unstable because the surface tension energy sink appears and disappears intermittently with the liquid emissions. In this case, one can say that surface tension stalls the steady jetting. The role played by viscosity in the tip is essentially different from that of surface tension. Viscous dissipation is present in that region as long as there are induced surface motions, and thus it survives even though the liquid emission is halted.

When the flow rate is decreased, the parameter that indicates which of σ or μ first enters into the scene is the capillary number $\text{Ca} = \mu U / \sigma$. For small Ca, surface tension stalls the flow first. The flow rate Q_σ and jet radius R_σ for which this occurs scale as

$$\sigma / R_\sigma \sim \Delta P \sim \rho Q_\sigma^2 / R_\sigma^4 \Rightarrow \begin{cases} Q_\sigma \sim \left(\dfrac{\sigma^4}{\rho \Delta P^3} \right)^{1/2} \\ R_\sigma \sim \sigma / \Delta P. \end{cases} \tag{6}$$

For simplicity, we define the minimum flow rate and the corresponding jet radius as

$$Q_\sigma = \left(\frac{\sigma^4}{\rho \Delta P^3}\right)^{1/2}, \quad R_\sigma = \sigma/\Delta P. \tag{7}$$

If $Q \simeq Q_\sigma$ then surface tension prevents the steady jetting regime from being reached.

For large Ca, viscosity affects the flow in the tip first. When viscosity enters the scene, the corresponding values Q_μ and R_μ of the flow rate and jet radius scale as

$$\mu Q_\mu/R_\mu^3 \sim \Delta P \sim \rho Q_\mu^2/R_\mu^4 \Rightarrow \begin{cases} Q_\mu \sim \left(\dfrac{\mu^4}{\rho^3 \Delta P}\right)^{1/2} \\ R_\mu \sim \left(\dfrac{\mu^2}{\rho \Delta P}\right)^{1/2}. \end{cases} \tag{8}$$

Analogously, we introduce the definitions

$$Q_\mu = \left(\frac{\mu^4}{\rho^3 \Delta P}\right)^{1/2}, \quad R_\mu = \left(\frac{\mu^2}{\rho \Delta P}\right)^{1/2}. \tag{9}$$

Equation (5) allows one to express the Weber, Reynolds, and capillary number (1) in terms of the flow rates Q_σ and Q_μ,

$$\mathrm{We} = \left(\frac{8}{\pi^2}\right)^{1/4}\left(\frac{Q}{Q_\sigma}\right)^{1/2}, \quad \mathrm{Re} = \left(\frac{2}{\pi^2}\right)^{1/4}\left(\frac{Q}{Q_\mu}\right)^{1/2},$$

$$\mathrm{Ca} = \sqrt{2}\left(\frac{Q_\mu}{Q_\sigma}\right)^{1/2}. \tag{10}$$

These definitions coincide with those introduced in Eq. (24) of [43].

The present study focuses on the wide parameter region of interest where viscous effects in the tapering region are smaller than or at most comparable to inertia and surface tension effects, i.e., for small to moderately large capillary numbers.

C. Energy balance in ES

We now apply the same arguments to ES. As in FF, we will neglect the role played by the surface tension and viscosity in the energy balance. ES is driven by Maxwell surface stress only. The variation in the normal component of that stress from the cone to the jet is on the order of $\varepsilon_0 E_n^2$, where E_n is the normal component of the electric field on the jet surface. Then, there is a suction effect equivalent to a drop pressure $\Delta P \sim \varepsilon_0 E_n^2$ along the cone. The tangential stress on the jet surface is $\tau_s = \varepsilon_0 E_n E_s$, where E_s is the tangential component of the electric field on the jet surface. If one compares τ_s with ΔP, one gets $\tau_s/\Delta P \sim E_s/E_n$. We are interested in the most general case in which $E_s \ll E_n$ on the jet, in accord with the leaky dielectric hypothesis [46]. This corresponds to most liquid solvents, water, etc. [7,31,47]. In this case, although their overall effect may become comparable due to the jet slenderness, tangential stresses are locally negligible compared with ΔP, and the electric potential decay ΔV is mainly converted into kinetic energy.

Taylor's electrostatic solution allows one to estimate the component of the electric field along the jet direction [47],

$$E_s \sim \left(\frac{\sigma}{\varepsilon_0 L}\right)^{1/2}, \tag{11}$$

where L is an axial characteristic length that is (i) small relative to the feeding capillary diameter, and (ii) long relative to the jet radius (see Fig. 2) [29,31,48]. A major fraction ΔV of the applied voltage V decays along the jet. We assume that this decay takes place mainly within the region limited by L, and thus

$$\Delta V \sim E_s L \sim \left(\frac{\sigma L}{\varepsilon_0}\right)^{1/2}. \tag{12}$$

In addition, the current intensity I conducted by the jet can be easily estimated as [7,31,37,47,49]

$$I \sim KR^2 E_s \sim KR^2 \left(\frac{\sigma}{\varepsilon_0 L}\right)^{1/2}. \tag{13}$$

Assuming that the electric potential decay is converted into kinetic energy, from Eqs. (12) and (13), one gets

$$\left.\begin{array}{l} I\Delta V \sim \dfrac{\sigma}{\varepsilon_0} KR^2 \sim \rho U^2 Q \\ U \sim Q/R^2 \end{array}\right\} \Rightarrow \begin{cases} R \sim \left(\dfrac{\rho Q^3 \varepsilon_0}{\sigma K}\right)^{1/6} \\ U \sim \left(\dfrac{\sigma K}{\rho \varepsilon_0}\right)^{1/3}. \end{cases} \tag{14}$$

We shall show in Sec. V that the scaling law for R obtained above from energy arguments agrees with most studies published since 1997 [7,26,29,31,47,50], while it differs from that proposed in [6,8]. Some salient features of Eq. (14) are as follows:

(i) The characteristic axial length L neatly cancels out from the analysis, making the scaling independent of additional electrohydrodynamic considerations in the neck-jet region (e.g., the possible relaxation of free charge onto the free surface). In particular, the scaling is independent of the liquid polarity and permittivity. The liquid polarity would enter the analysis if the inner electric field was comparable to the externally applied one. This would be so if high rates of charge injection onto the free surface were demanded, which occurs in UTS but not in STS. Owing to the jet's slenderness, the radial electric field in the jet is smaller than the axial one. The latter is of the same order as the electric field on the meniscus surface [7] and much smaller than the external normal electric field on the jet's free surface. Therefore, one expects that the inner radial electric field, and consequently the liquid permittivity, would not be involved in the mechanisms governing the jet size.

(ii) The proposed scaling is independent of the applied voltage. This is so because the size of the transition region is sufficiently small relative to that of the meniscus, whose geometry indeed is affected by the total applied voltage V.

(iii) Surface tension appears in Eq. (14) because of its influence on the meniscus shape only. To derive Eq. (14), one considers the electric field E_s, whose value depends on the meniscus shape. The meniscus shape is the result of the balance between the pressure jump across the free surface, surface tension, and Maxwell stresses. For this reason, jet radius

(14) depends on σ. It must be noted that the surface tension does not appear in Eq. (14) because of its direct role in the jet dynamics. In fact, the effects of the surface tension on the jet are negligible compared to those of the liquid inertia in most experiments.

We now focus on the mechanical aspect of the ES problem. The liquid is ultimately driven by an effective pressure drop ΔP that fuels its inertia. If one again neglects the effects of surface tension and viscosity, then ΔP can be estimated as $\Delta P \sim \rho U^2$. From Eq. (14), one gets

$$\Delta P \sim \left(\frac{\sigma^2 K^2 \rho}{\varepsilon_0^2} \right)^{1/3}. \tag{15}$$

Interestingly, ΔP is a function of the liquid properties (and ε_0) only [31] and does not depend on the applied voltage V. As mentioned above, this quantity affects the *global* shape of the quasielectrostatic meniscus. However, the flow is set in motion *locally*, in the neck region, where its structure is not significantly affected by the meniscus shape.

Equation (15) shows that the applied voltage (and the rest of the quantities absent in that equation) affects the flow behavior in the neck region to a lesser extent. For this reason, we shall assume that ΔP obeys the universal expression

$$\Delta P = k_p \left(\frac{\sigma^2 K^2 \rho}{\varepsilon_0^2} \right)^{1/3}, \tag{16}$$

where k_p is a constant of order unity. It is worth emphasizing again that σ appears in Eq. (16) due to its influence on the meniscus shape and consequently on the electric field acting along the jet direction; the effects of σ on the jet dynamics are negligible relative to inertia.

Equation (16) constitutes the link between ES and FF. One can consider the electrical quantities K and ε_0 as *effective* operational parameters in ES. Equation (16) allows one to determine the corresponding driven pressure drop ΔP as a function of those parameters exclusively. The value of the constant k_p is estimated as explained in Sec. IV B. The energy balance between the pressure drop and kinetic energy described in Sec. II B for FF also holds in the ES atomization. Therefore, the pressure drop [Eq. (16)] and the flow rate Q also verify scaling laws (4), (6), and (8). One can also apply to the ES problem definitions (7) and (9) of the limiting values of the flow rate and jet radius. The ES problem can also be described in terms of the Weber, Reynolds, and capillary numbers given by Eq. (10).

D. Common similarity law for the jet radius in ES and FF

Equation (5) allows one to estimate the issuing jet radius R from the parameters $\{\rho, Q, \Delta P\}$ in both ES and FF atomizations. In the steady jetting regime, the jet breaks up into droplets downstream due to the Rayleigh instability [9]. The radius R_d of the resulting droplets is proportional to the jet radius and is determined by the wavelength of the perturbation with maximum growth rate. As a first approximation, one can assume that the viscosity and the existence of surface stresses and electric charges do not significantly alter the wavelength of the perturbation with maximum growth

TABLE I. Liquids focused with air or nitrogen. The properties were measured at 25 °C. The viscosity and surface tension were measured with a Brookfield viscometer mod. LVDV-II+UL spindle and a digital Krüss tensiometer.

Liquid	Ref.	ρ (kg m^{-3})	σ (N m^{-1})	μ (Pa s)
Water	[45]	998	0.072	0.0011
Water+10% ethanol		982	0.0475	0.0015
Ethanol	[45]	789	0.023	0.0012
Water+1% alginate		1000	0.069	0.0213
Water+2% alginate		1000	0.069	0.1005

rate at least for low and moderately high Weber numbers. Although this assumption requires a second-order revision (see, e.g., [51]), that revision does not change the conclusions of the present analysis. Then, the droplet radius R_d only depends on $\{\rho, Q, \Delta P\}$ in both ES and FF; more specifically,

$$\frac{R_d}{(\rho Q^2/\Delta P)^{1/4}} = K_d. \tag{17}$$

In FF, K_d is a nearly universal constant. Following the usual definition of a *self-similar* phenomenon (pp. 82–89 of [52]), one can assert that FF atomization exhibits nearly complete self-similarity. Now, if one assumes that k_p in Eq. (16) is a nearly universal constant, then so is K_d in ES. In this case, ES atomization also exhibits nearly complete self-similarity, and one can assert that FF and ES verify equivalent similarity laws.

In Secs. III and V, we will provide solid support for the arguments that have been presented in this section on the basis of experiments conducted in this work and a very large number of results garnered from the literature. In particular, we will test in Sec. III whether the flow rate limit Q_σ is observed in real practice of both FF and ES. In Sec. V, we will test experimentally whether similarity law (17) for the droplet size is verified in the two atomization techniques.

III. PARAMETER REGION OF STEADY JETTING

A. Flow focusing

FF experiments were conducted by using "classical" axisymmetric flow focusing arrangements with different sizes [45]. Liquids with very different viscosities were nebulized, observing the jet stability and measuring the droplet size distribution in the case of water and ethanol. The properties of the liquids are shown in Table I.

Figure 3 shows the projection of the FF data on the (We,Ca) plane. The vertical black line is the global stability limit, We=1. This means that $Q=Q_\sigma$ constitutes a lower limit of Q for all liquids and geometrical configurations. The flow rate Q must be larger than Q_σ, otherwise the liquid cannot go uphill over the pressure maximum (proportional to σ/R) caused by the stagnation point at the neck. In other words, the energy injected into the liquid must exceed that consumed in the production of the free surface. This limita-
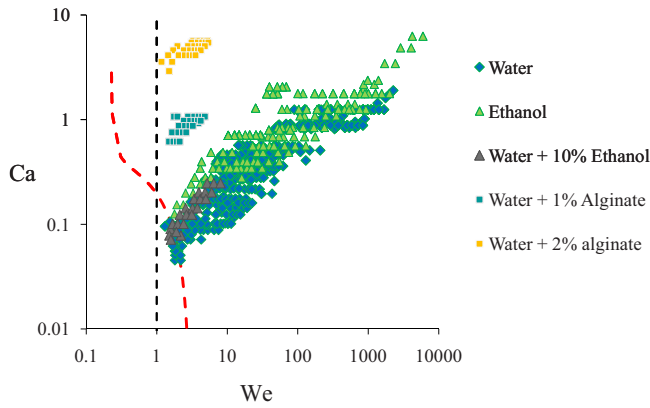
FIG. 3. (Color online) Projection of the FF data on the (We,Ca) plane. The symbols correspond to the liquids in Table I. The curved (red online) line represents the convective/absolute instability transition of the jet, while the black line shows the limit We=1.

tion should be present in both FF and ES since it is independent of the global flow structure and the meniscus shape. Much care was taken in the experiments for flow rates close to Q_σ, as explained in the experimental section in [43]. The curved line in Fig. 3 corresponds to the convective/absolute instability transition obtained analytically for a cylindrical liquid jet in an environment of much lower density and viscosity (see, e.g., [12,53]). As can be observed, this line constitutes an additional stability limit for the steady jetting regime. A portion of the liquid jet close to the neck must be locally stable, which in general means that perturbations growing in time must be convected downstream by the liquid stream (convective instability). There are points lying slightly below the red line. This is consistent with the fact that, owing to the coflowing gas stream, the jet free surface is moving with a velocity slightly greater than that of the bulk, which naturally favors the jet to sweep growing surface waves downstream [54,55], displacing the onset of dripping to lower flow rates.

It is worth noting that the flow rate Q_μ given by Eq. (9) merely labels the flow conditions for which inertia and viscous forces become comparable.

B. Electrospray

A number of ES experiments have been conducted in the past using different liquids. In the present work, we have collected and analyzed about 1300 measurements from the literature, including results for 63 liquids electrosprayed in the steady cone-jet regime by many different authors since 1987. The liquid properties are summarized in Tables II–V according to their electrical properties (K and ε) and chemical similarity. Table II corresponds to common organic solvents, Tables III and IV correspond to moderate and high permittivity (polar) liquids, and Table V to liquid mixtures consisting fundamentally of two liquids with disparate permittivities used to study the effect of a varying liquid permittivity. Specifically, data for water (with $K=0.015$, 0.09, 0.15, and 1.8 S/m) and for 3-ethylene and 4-ethylene glycol have kindly been supplied by López-Herrera *et al.* [36] and by Rosell-Llompart and Fernandez de la Mora [25], respectively. Data for the ionic liquid mixtures EMI-Im (Gam, PoF) and EMI-Im (Gam, JFM) were kindly provided by Gamero and published in [56,57], respectively.

The parameters ΔP, U, R_σ, R_μ, Q_σ, and Q_μ can be calculated from the scaling laws proposed in Sec. II as a function of the liquid properties. The results are given in Tables VI–IX. It must be emphasized that ΔP is not an operational parameter in ES. Its value is obtained from Eq. (16) as a function of the electrical properties K and ε_0. The small effect of the rest of the electrical parameters on the phenomenon is reduced to a constant k_p of order unity. One can neglect that effect and assume that k_p takes a nearly universal value in ES experiments. Then, both ES and FF atomizations exhibit nearly complete self-similarity, and the droplet size must verify similarity law (17).

To calculate k_p, we resort to the experimental results reported in [50,57,58], which are some of the most careful

TABLE II. Properties of some organic solvents.

Liquid	Ref.	ρ (kg m^{-3})	σ (N m^{-1})	ε	K (S m^{-1})	μ (Pa s)
Heptane 1	[47]	684	0.021	1.9	7.72×10^{-7}	0.00039
Heptane 2	[47]	684	0.021	1.9	1.90×10^{-6}	0.00039
Heptane 3	[47]	684	0.021	1.9	4.50×10^{-6}	0.00039
Dioxane+FM (1)	[24]	1030	0.031	2.4	3.20×10^{-6}	0.00139
Dioxane 2% FM	[47]	1030	0.03	2.3	2.40×10^{-7}	0.00139
Dioxane 4% FM	[47]	1030	0.031	2.5	1.10×10^{-6}	0.00139
Dioxane+stadis	[47]	1030	0.03	2.2	5.00×10^{-7}	0.00139
Isopar+15% n-butOH	[23]	754.75	0.024	2.64	7.14×10^{-9}	0.00173
Isopar+20% n-butOH	[23]	758	0.024	3.06	3.85×10^{-8}	0.0018
Isopar+25% n-butOH	[23]	761.25	0.024	3.56	1.33×10^{-7}	0.00188
Isopar+30% n-butOH	[23]	764.5	0.024	5.2	4.00×10^{-7}	0.00195
Isopar+35% n-butOH	[23]	767.75	0.024	7	1.25×10^{-6}	0.00203
Isopar+40% n-butOH	[23]	771	0.024	10	2.22×10^{-6}	0.0021

TABLE III. Properties of some liquids with moderate permittivity.

Liquid	Ref.	ρ (kg m^{-3})	σ (N m^{-1})	ε	K (S m^{-1})	μ (Pa s)
Methanol	[47]	795	0.021	33.6	8.50×10^{-5}	0.00059
Ethanol		795	0.0226	24.55	3.50×10^{-5}	0.00120
Butanol	[47]	800	0.023	17.84	7.50×10^{-6}	0.00254
Octanol	[47]	827	0.024	9.93	1.14×10^{-6}	0.00720
Octanol 1	[8]	825.5	0.026	10.34	1.16×10^{-3}	0.008
n-butanol 1	[26]	810	0.0246	17.8	1.50×10^{-5}	0.00294
Acetone	[47]	790	0.023	20.7	5.30×10^{-5}	0.00032
2-butanona	[65]	805.4	0.0246	18.5	4.50×10^{-5}	0.00042
Ethylene glycol 1	[8]	1110	0.0484	38.66	2.40×10^{-1}	0.021
Ethylene glycol 2	[8]	1110	0.0484	38.66	6.26×10^{-2}	0.021
Ethylene glycol 3	[8]	1110	0.0484	38.66	1.69×10^{-2}	0.021
Ethylene glycol 4	[8]	1110	0.0484	38.66	5.00×10^{-4}	0.021
3-ethyl. glyc. (a)	[25]	1134	0.0454	23.7	3.35×10^{-4}	0.0366
3-ethyl. glyc. (b)	[25]	1134	0.0454	23.7	1.27×10^{-3}	0.0366
3-ethyl. glyc. (c)	[25]	1134	0.0454	23.7	2.73×10^{-3}	0.0366
3-ethyl. glyc. (d)	[25]	1134	0.0454	23.7	5.04×10^{-3}	0.0366
3-ethyl. glyc. (e)	[25]	1134	0.0454	23.7	1.58×10^{-2}	0.0366
4-ethyl. glyc. (a)	[25]	1137	0.0448	20.5	7.38×10^{-3}	0.0456
4-ethyl. glyc. (b)	[25]	1137	0.0448	20.5	3.70×10^{-2}	0.0456

attempts to reach the minimum issued liquid flow rates in ES. In the first study [50], the authors used a thin wire to minimize the flow recirculation and stabilize the tapering meniscus. The second study [58] provides what is possibly the most interesting data for our purposes. In this case, the authors get so close to the minimum attainable liquid flow rate that, for the lowest value reported, the issued charge flow is almost entirely made of ions. The constant k_p is calculated under the requirement that the parameter regions of the FF results and the ES data reported in these three studies exhibit the same boundaries. Remarkable agreement was obtained for $k_p \simeq 1.3$.

TABLE IV. Properties of some liquids with high permittivity.

Liquid	Ref.	ρ (kg m^{-3})	σ (N m^{-1})	ε	K (S m^{-1})	μ (Pa s)
Water ($K=0.015$)	[36]	998	0.072	80	1.50×10^{-2}	0.001
Water ($K=0.09$)	[36]	998	0.067	80	7.00×10^{-2}	0.001
Water ($K=0.15$)	[36]	998	0.072	80	1.50×10^{-1}	0.001
Water ($K=1.8$)	[36]	998	0.055	80	2.20	0.001
Water 1	[8]	1000	0.0726	80.1	8.30×10^{-1}	0.001
Water 2	[8]	1000	0.0726	80.1	9.26×10^{-2}	0.001
Water 3	[8]	1000	0.0726	80.1	2.13×10^{-2}	0.001
Water 4	[8]	1000	0.0726	80.1	2.15×10^{-3}	0.001
Water+glucose 1	[30]	1000	0.072	80.1	1.08×10^{-1}	0.001
Water+glucose 2	[30]	1000	0.072	80.1	2.99×10^{-2}	0.001
Water+glucose 3	[30]	1000	0.072	80.1	7.72×10^{-3}	0.001
Water+ glucose 4	[30]	1000	0.072	80.1	2.19×10^{-3}	0.001
Formamide 1	[8]	1130	0.058	111	1.00×10^{-1}	0.00376
Formamide 2	[8]	1130	0.058	111	5.50×10^{-2}	0.00376
Formamide 3	[8]	1130	0.058	111	3.16×10^{-2}	0.00376
Formamide 4	[8]	1130	0.058	111	2.84×10^{-2}	0.00376
Formamide	[67]	1130	0.058	111	6.12×10^{-1}	0.00376

TABLE V. Properties of ionic liquids and mixtures with varying permittivity.

Liquid	Ref.	ρ (kg m^{-3})	σ (N m^{-1})	ε	K (S m^{-1})	μ (Pa s)
EMI-Im	[56]	1520	0.0349	3	8.80×10^{-1}	0.034
EMI-Im	[57]	1200	0.0419	65	1.70×10^{-3}	0.00276
EtNH3-COOH	[66]	1100	0.04	3	1.40	0.01
TBP+Emi-Im/TBTP	[29]	976	0.028	8.91	2.20×10^{-2}	0.00359
TBP+TBTP 1	[29]	976	0.028	8.91	8.53×10^{-3}	0.00359
TBP+TBTP 2	[29]	976	0.028	8.91	1.64×10^{-3}	0.00359
TBP+TBTP 3	[29]	976	0.028	8.91	5.34×10^{-4}	0.00359
TBP+TBTP 4	[29]	976	0.028	8.91	2.30×10^{-4}	0.00359
PC-EMI-BF4	[58]	1200	0.042	65	1.04	0.00276
MeOH/H2O/OHAc	[50]	1030	0.037	55	1.35×10^{-4}	0.008
Dioxane 10% W	[47]	1027	0.033	6.25	4.50×10^{-6}	0.00157
Dioxane 25% W	[47]	1022	0.037	14.2	1.70×10^{-4}	0.00205
Dioxane 50% W	[47]	1015	0.043	34.5	5.70×10^{-4}	0.00235
Dioxane 66.7% W	[47]	1010	0.044	49.1	1.30×10^{-3}	0.00195

The flow structure in the neck-jet region exhibits common features in ES and FF and is not significantly affected by the meniscus shape or the configuration geometry. Consequently, one may expect common stability limits for the steady jetting regime established by the surface tension forces at that region. Figure 4 shows the projection on the (We,Ca) plane of all the data, with the exception of those of low viscosity organic solvents (Table II). The ES data are superimposed on those of FF (Fig. 3), showing good agreement between the parameter regions of steady jetting. These regions are limited by the boundary We=1 in both cases. It must be noted that use was made of Eq. (14) to calculate We and Ca even for large values of Ca despite viscous forces were important in that case. We chose to include these data because the corresponding droplet diameter measurements, when available

[56], agreed with Eq. (14) (see Sec. V).

Low viscosity and moderately low conductivity liquids (Table II) exhibit particular behaviors in ES that merit separate analysis. Figure 5 shows the projection of the data obtained from [50,58] on the (We,Ca) plane. One observes a clear departure of the data from the boundary We=1 for Ca$\lesssim$0.1, which demands a more detailed inquiry into the fluidic structure of the jets in this limit. In particular, one must consider the role played by the thin boundary layers in the jet for small Ca. In this limit, the velocity on the jet free surface is larger than the mean jet velocity. Consequently, the perturbations are convected downstream by higher speeds, which allows one to reach significantly smaller values of the flow rate and Weber number [54,55]. The specific analysis of this case is beyond the scope of the present paper.

TABLE VI. Properties of some organic solvents.

Liquid	Ref.	ΔP (Pa)	U (m s^{-1})	R_σ (m)	Q_σ (m^3 s^{-1})	Ca
Heptane 1	[47]	1.71×10^{3}	2.24	1.22×10^{-5}	2.37×10^{-10}	4.16×10^{-2}
Heptane 2	[47]	3.13×10^{3}	3.02	6.72×10^{-6}	9.65×10^{-11}	5.61×10^{-2}
Heptane 3	[47]	5.55×10^{3}	4.03	3.78×10^{-6}	4.07×10^{-11}	7.48×10^{-2}
Dioxane+FM (1)	[24]	6.58×10^{3}	3.57	4.71×10^{-6}	5.62×10^{-11}	1.60×10^{-1}
Dioxane 2% FM	[47]	1.14×10^{3}	1.49	2.62×10^{-5}	7.25×10^{-10}	6.91×10^{-2}
Dioxane 4% FM	[47]	3.23×10^{3}	2.50	9.61×10^{-6}	1.63×10^{-10}	1.12×10^{-1}
Dioxane+stadis	[47]	1.87×10^{3}	1.90	1.61×10^{-5}	3.48×10^{-10}	8.82×10^{-2}
Isopar+15% n-but OH	[23]	8.53×10^{1}	4.76×10^{-1}	2.81×10^{-4}	2.66×10^{-8}	3.42×10^{-2}
Isopar+20% n-but OH	[23]	2.63×10^{2}	8.33×10^{-1}	9.13×10^{-5}	4.91×10^{-9}	6.25×10^{-2}
Isopar+25% n-but OH	[23]	6.01×10^{2}	1.26	3.99×10^{-5}	1.42×10^{-9}	9.82×10^{-2}
Isopar+30% n-but OH	[23]	1.25×10^{3}	1.81	1.91×10^{-5}	4.69×10^{-10}	1.47×10^{-1}
Isopar+35% n-but OH	[23]	2.69×10^{3}	2.65	8.93×10^{-6}	1.49×10^{-10}	2.23×10^{-1}
Isopar+40% n-but OH	[23]	3.94×10^{3}	3.20	6.08×10^{-6}	8.37×10^{-11}	2.80×10^{-1}

TABLE VII. Properties of some liquids with moderate permittivity.

Liquid	Ref.	ΔP (Pa)	U (m s^{-1})	R_σ (m)	Q_σ (m^3 s^{-1})	Ca
Methanol	[47]	4.14×10^4	1.02×10^1	5.07×10^{-7}	1.86×10^{-12}	2.87×10^{-1}
Ethanol		2.41×10^4	7.78	9.39×10^{-7}	4.85×10^{-12}	4.13×10^{-1}
Butanol	[47]	8.74×10^3	4.67	2.63×10^{-6}	2.29×10^{-11}	5.16×10^{-1}
Octanol	[47]	2.59×10^3	2.50	9.27×10^{-6}	1.52×10^{-10}	7.51×10^{-1}
Octanol 1	[8]	2.76×10^5	2.59×10^1	9.41×10^{-8}	1.62×10^{-13}	7.96
n-butanol 1	[26]	1.46×10^4	6.00	1.69×10^{-6}	1.21×10^{-11}	7.17×10^{-1}
Acetone	[47]	3.21×10^4	9.01	7.18×10^{-7}	3.28×10^{-12}	1.25×10^{-1}
2-butanona	[65]	3.03×10^4	8.67	8.13×10^{-7}	4.05×10^{-12}	1.47×10^{-1}
Ethylene glycol 1	[8]	1.61×10^7	1.71×10^2	3.00×10^{-9}	1.08×10^{-15}	7.40×10^1
Ethylene glycol 2	[8]	6.59×10^6	1.09×10^2	7.35×10^{-9}	4.16×10^{-15}	4.73×10^1
Ethylene glycol 3	[8]	2.75×10^6	7.04×10^1	1.76×10^{-8}	1.54×10^{-14}	3.06×10^1
Ethylene glycol 4	[8]	2.63×10^5	2.18×10^1	1.84×10^{-7}	5.21×10^{-13}	9.45
3-ethyl. glyc. (a)	[25]	1.94×10^5	1.85×10^1	2.33×10^{-7}	7.14×10^{-13}	1.49×10^1
3-ethyl. glyc. (b)	[25]	4.73×10^5	2.89×10^1	9.60×10^{-8}	1.88×10^{-13}	2.33×10^1
3-ethyl. glyc. (c)	[25]	7.88×10^5	3.73×10^1	5.76×10^{-8}	8.76×10^{-14}	3.00×10^1
3-ethyl. glyc. (d)	[25]	1.19×10^6	4.57×10^1	3.83×10^{-8}	4.74×10^{-14}	3.69×10^1
3-ethyl. glyc. (e)	[25]	2.54×10^6	6.69×10^1	1.79×10^{-8}	1.51×10^{-14}	5.39×10^1
4-ethyl. glyc. (a)	[25]	1.52×10^6	5.16×10^1	2.95×10^{-8}	3.19×10^{-14}	5.26×10^1
4-ethyl. glyc. (b)	[25]	4.44×10^6	8.84×10^1	1.01×10^{-8}	6.36×10^{-15}	9.00×10^1

IV. OTHER LIMITING MECHANISMS IN FF

A. Tangential stresses on the meniscus: A mechanism setting a minimum pressure drop for FF

There are obvious differences in how momentum is transferred across the meniscus free surface in ES and FF. Those differences become clear at length scales sufficiently large compared to that of the neck-jet region. Consider a characteristic length $D \gg R$ of the ES or FF geometrical configuration. D is the feeding tube diameter in ES and the orifice diameter in FF and sets the spatial scale of the external fields (the outer electric field in ES and the gas stream in FF).

TABLE VIII. Properties of some liquids with high permittivity.

Liquid	Ref.	ΔP (Pa)	U (m s^{-1})	R_σ (m)	Q_σ (m^3 s^{-1})	Ca
Water ($K=0.015$)	[36]	3.20×10^6	8.00×10^1	2.25×10^{-8}	2.87×10^{-14}	1.11
Water ($K=0.09$)	[36]	8.51×10^6	1.31×10^2	7.88×10^{-9}	5.73×10^{-15}	1.95
Water ($K=0.15$)	[36]	1.48×10^7	1.72×10^2	4.85×10^{-9}	2.87×10^{-15}	2.39
Water ($K=1.8$)	[36]	7.43×10^7	3.86×10^2	7.40×10^{-10}	1.50×10^{-16}	7.02
Water 1	[8]	4.67×10^7	3.06×10^2	1.55×10^{-9}	5.22×10^{-16}	4.21
Water 2	[8]	1.08×10^7	1.47×10^2	6.71×10^{-9}	4.68×10^{-15}	2.03
Water 3	[8]	4.06×10^6	9.01×10^1	1.79×10^{-8}	2.04×10^{-14}	1.24
Water 4	[8]	8.81×10^5	4.20×10^1	8.24×10^{-8}	2.02×10^{-13}	5.78×10^{-1}
Water+glucose 1	[30]	1.19×10^7	1.54×10^2	6.04×10^{-9}	3.98×10^{-15}	2.14
Water+glucose 2	[30]	5.07×10^6	1.01×10^2	1.42×10^{-8}	1.44×10^{-14}	1.40
Water+glucose 3	[30]	2.05×10^6	6.41×10^1	3.51×10^{-8}	5.57×10^{-14}	8.90×10^{-1}
Water+glucose 4	[30]	8.87×10^5	4.21×10^1	8.12×10^{-8}	1.96×10^{-13}	5.85×10^{-1}
Formamide 1	[8]	1.02×10^7	1.34×10^2	5.68×10^{-9}	3.06×10^{-15}	8.72
Formamide 2	[8]	6.86×10^6	1.10×10^2	8.46×10^{-9}	5.57×10^{-15}	7.14
Formamide 3	[8]	4.74×10^6	9.16×10^1	1.22×10^{-8}	9.70×10^{-15}	5.94
Formamide 4	[8]	4.41×10^6	8.84×10^1	1.31×10^{-8}	1.08×10^{-14}	5.73
Formamide	[67]	3.42×10^7	2.46×10^2	1.70×10^{-9}	5.01×10^{-16}	1.59×10^1

TABLE IX. Properties of some ionic liquids and mixtures with varying permittivity.

Liquid	Ref.	ΔP (Pa)	U (m s^{-1})	R_σ (m)	Q_σ (m^3 s^{-1})	Ca
EMI-Im	[56]	3.43×10^7	2.12×10^2	1.02×10^{-9}	1.56×10^{-16}	2.07×10^2
EMI-Im	[57]	5.55×10^5	3.04×10^1	7.55×10^{-8}	1.23×10^{-13}	2.00
EtNH3-COOH	[66]	4.59×10^7	2.89×10^2	8.71×10^{-10}	1.55×10^{-16}	7.22×10^1
TBP+Emi-Im/TBTP	[29]	2.18×10^6	6.69×10^1	1.28×10^{-8}	7.79×10^{-15}	8.57
TBP+TBTP 1	[29]	1.16×10^6	4.88×10^1	2.41×10^{-8}	2.01×10^{-14}	6.25
TBP+TBTP 2	[29]	3.86×10^5	2.81×10^1	7.24×10^{-8}	1.04×10^{-13}	3.61
TBP+TBTP 3	[29]	1.83×10^5	1.94×10^1	1.53×10^{-7}	3.21×10^{-13}	2.48
TBP+TBTP 4	[29]	1.04×10^5	1.46×10^1	2.68×10^{-7}	7.45×10^{-13}	1.87
PC-EMI-BF4	[58]	4.00×10^7	2.58×10^2	1.05×10^{-9}	2.01×10^{-16}	1.70×10^1
MeOH/H2O/OHAc	[50]	8.97×10^4	1.32×10^1	4.13×10^{-7}	1.59×10^{-12}	2.85
Dioxane 10% W	[47]	8.60×10^3	4.09	3.84×10^{-6}	4.26×10^{-11}	1.95×10^{-1}
Dioxane 25% W	[47]	1.04×10^5	1.43×10^1	3.55×10^{-7}	1.27×10^{-12}	7.92×10^{-1}
Dioxane 50% W	[47]	2.58×10^5	2.25×10^1	1.67×10^{-7}	4.44×10^{-13}	1.23
Dioxane 66.7% W	[47]	4.53×10^5	2.99×10^1	9.72×10^{-8}	2.00×10^{-13}	1.33

Consider first a FF experiment characterized by a small pressure drop ΔP. Suppose that there is a quasistatic solution for the meniscus shape with a rounded apex. In this case, the tangential surface stresses are not sufficient to overcome the surface tension stress, which is simply balanced by the difference between the pressures of the stagnation regions located at both the liquid and gas sides of the apex. Because a liquid flow rate Q is being injected through the capillary, the meniscus will approach slowly the orifice until the pressure imbalance along the whole meniscus causes its breakup, and an unsteady liquid ejection in the form of droplets occurs (see Fig. 14 of [43]). Figure 6(a) illustrates this first possibility.

For sufficiently large values of the pressure drop ΔP, the meniscus evolution is however different. The pressure drop ΔP accelerates the gas stream. If the resulting viscous tangential stresses τ_s on the meniscus surface are sufficiently large compared with σ/D, then the meridional flow driven by them will eventually deform the interface, the deformation will increase along the meniscus meridian as the liquid approaches the neck, and the meniscus will become extruded in the form of a thin jet according to mass conservation. A steady tapering meniscus will then be possible as long as a steady liquid flow rate Q is injected [39]. Figure 6(b) illustrates this second possibility. Viscous tangential stresses are, therefore, a necessary ingredient to get steady tip streaming
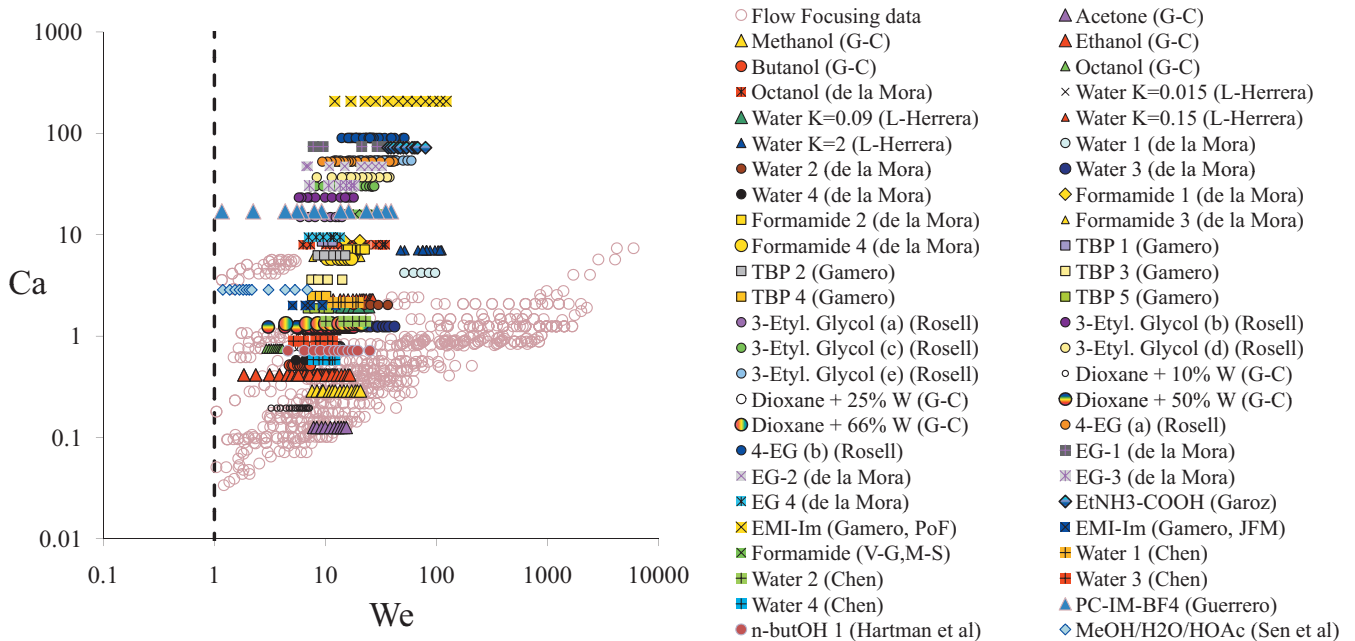

FIG. 4. (Color) Projection of the experimental conditions for steady jetting on the (We,Ca) plane for both FF and ES. The dashed line is the stability limit We=1.
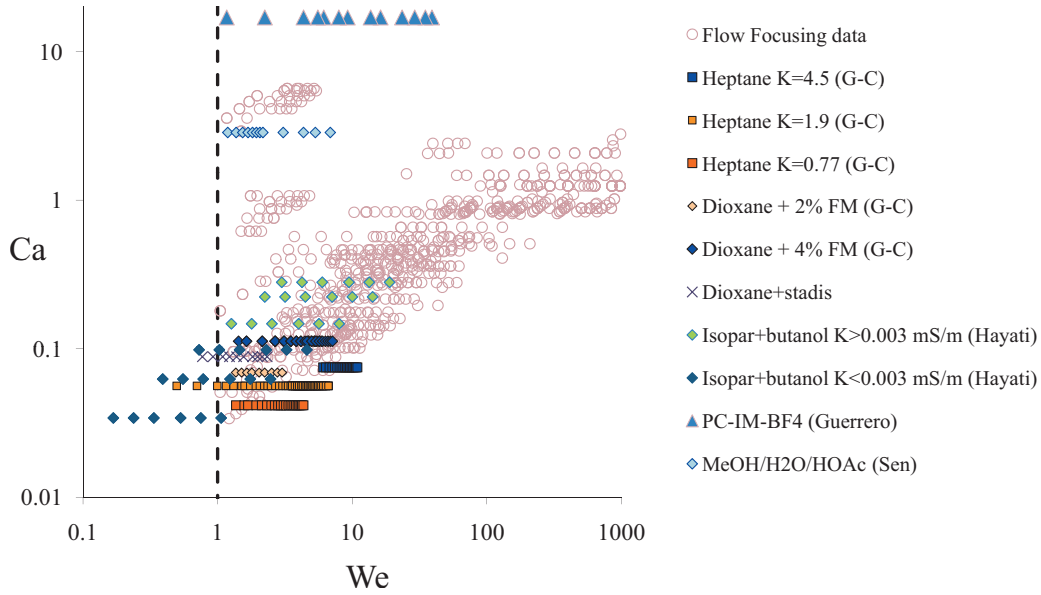
FIG. 5. (Color) Projection of the experimental conditions for steady jetting on the (We,Ca) plane for low viscosity and moderately low conductivity liquids (Table II). The vertical line is the stability limit, We=1.

although they do not contribute significantly to the global energy balance in the steady jetting regime (see Sec. II B).

We have described above a limiting mechanism which involves the action of the tangential viscous stresses τ_s on the FF meniscus surface at scales on the order of D. It is therefore natural to interrogate the system about the relative importance of τ_s and the surface tension stress σ/D at that scale. We seek for typical values of the parameter

$$Z = \tau_s D / \sigma. \tag{18}$$

From Eq. (2), one gets
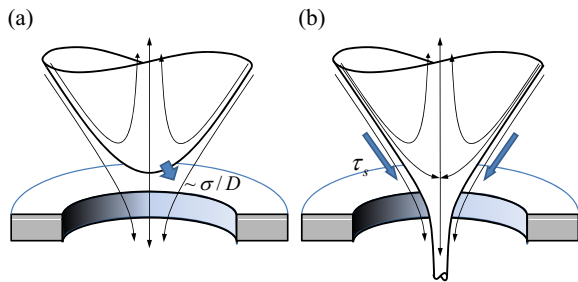
FIG. 6. (Color online) The role of the tangential viscous stress in establishing a steady meniscus shape in FF. (a) In the absence of a sufficiently strong tangential stress, a round-apex meniscus is obtained. Both the inner liquid and the external gas flows would exhibit stagnation regions around the round apex. The surface tension stress σ/D would be simply balanced by an appropriate pressure jump across the interface. If one slowly pushes a liquid flow rate Q, the system would spit intermittently the excess of liquid to recover the round-apex equilibrium shape. (b) However, when the tangential stress is sufficiently vigorous compared to σ/D, the surface can be deformed into a steady tapering shape, which allows the continuous and smooth acceleration of the liquid under the combined actions of the pressure drop ΔP and the tangential viscous stress τ_s on the liquid surface.

$$Z \sim \left(\frac{D^2 \Delta P^3 \mu_g^2}{\rho_g \sigma^4} \right)^{1/4}. \tag{19}$$

Note that Z depends on the imposed pressure drop ΔP but not on the flow rate Q. Figure 7 shows the values of Z as a function of We. The figure depicts the global limits of the operational parameters set by the surface tension and the tangential viscous stresses on the meniscus surface (related to ΔP). Steady jetting was found for We$\gtrsim 1$ and $Z \gtrsim 0.33$. Figure 8 shows two additional projections of the data on the parameter planes (Z, Ca) and (Z, Re). The global stability limit $Z \simeq 0.33$ is independent of the parameters of the jet, which indicates that the origin of the instability is external to the jet.

At this point, one would wonder whether a limiting mechanism similar to that described above for FF can be found in ES. In ES, tangential electric and viscous stresses are nearly balanced at the cone surface. The same occurs
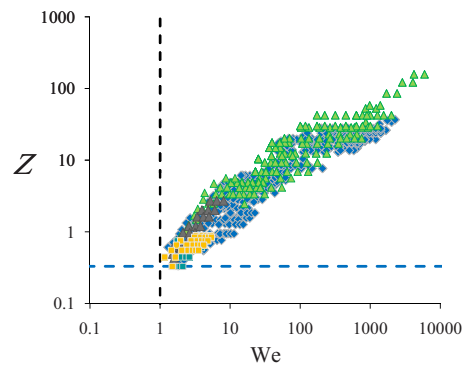
FIG. 7. (Color online) The parameter Z as a function of We for FF. The symbols are those of Fig. 3. The vertical and horizontal lines are the global stability limits We=1 and $Z \simeq 0.33$ of the meniscus, respectively.
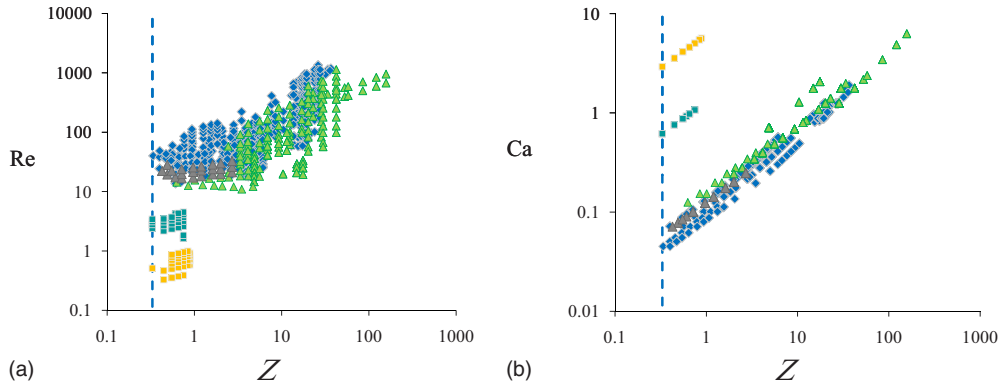
FIG. 8. (Color online) Re and Ca as a function of Z for FF. The symbols are those of Fig. 3. The vertical line is the global stability limit $Z=0.33$.

with the normal electric and surface tension stresses [33]. Therefore, Z in ES is simply the ratio of the tangential to the normal component of the electric field at the cone surface,

$$Z \equiv \tau_s D/\sigma \sim \varepsilon_0 E_n^{\mathrm{cone}} E_s^{\mathrm{cone}} D/\sigma \sim E_s^{\mathrm{cone}}/E_n^{\mathrm{cone}} \sim \left(\frac{\varepsilon_0 I^2}{K^2 \sigma D^3} \right)^{1/2}. \tag{20}$$

Figure 9 shows the projection on the (Z, We) plane of the FF (Fig. 5) and ES data. Both FF and ES stability regions are limited by the vertical line We=1. The figure, however, reveals a fundamental difference between FF and ES. The horizontal line corresponding to the tangential stress limiting mechanism in FF does not apply to ES. Much on the contrary, tangential stresses are significantly smaller than the surface tension stresses on the ES cone surface. This is consistent with the fact that the action of the gas stream in FF cannot lead to a steady meniscus with zero curvature at the apex and no liquid emission. The physical picture is entirely different in ES. The Taylor solution (cone) and further refinements including the effects of the needle and the electrode [33] provide the perfect framework of a tapering shape when a liquid flow rate is injected through the needle. In other words, ES does not need tangential stresses on the meniscus surface to issue a thin jet because the normal electric field almost balances surface tension down to any imaginably
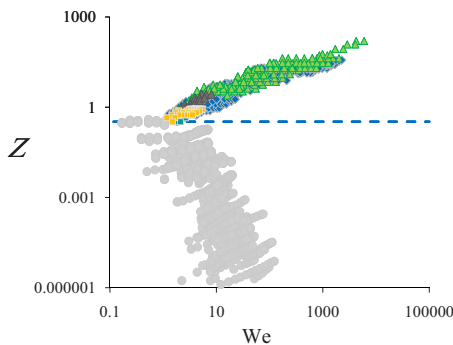
small scale. On the contrary, tangential stresses strive in FF against surface tension to produce and keep running a steady cusplike meniscus.

B. Recirculating flow pattern: A mechanism setting a minimum flow rate for FF

We should investigate whether the recirculating flow pattern caused by the tangential viscous stresses is another fundamental feature of FF. According to the findings of Herrada *et al.* [43], when the Reynolds number based on D,

$$\mathrm{Re}_D = \frac{\rho Q}{\mu D}, \tag{21}$$

is sufficiently large (say, $\mathrm{Re}_D \gtrsim 10$), there is a critical flow rate Q_r below which one finds a recirculation cell and a stagnation point in the neck region where the pressure reaches a local maximum. This fluidic structure is a consequence of the accumulation of momentum in the neck region due to the action on the free surface meniscus of the external gas stream. In other words, the energy injected through the meniscus free surface by the external gas flow accumulates in the apex and is evacuated by the recirculation cell. The pressure and location of the stagnation point depend on the configuration of the gas stream and thus on the geometrical parameters.

Numerical simulations of FF [43] have shown that the flow rate Q_r at the onset of recirculation scales as

$$Q_r \sim Q_D \equiv \frac{D\mu}{\rho}, \tag{22}$$

and the size S_r of the recirculation cell can be estimated from the expression

$$S_r = C_1 R_1 - C_2 \frac{\rho Q}{\mu}, \tag{23}$$

where R_1 is the inner radius of the feeding capillary. In Eq. (22), Q_D was defined so that $\mathrm{Re}_D = Q/Q_D$. For low viscosity liquids (i.e., large Re_D), the boundary layer near the free surface is small relative to the cell size, and the constants C_1 and C_2 depend on the geometrical parameters only. It is natural to hypothesize that the cell size S_r cannot be much larger

FIG. 9. (Color online) Z as a function of We for FF and ES. The symbols are those of Fig. 3. The horizontal line is the global stability limit $Z=0.33$ for FF. The gray solid circles correspond to the ES data [59].
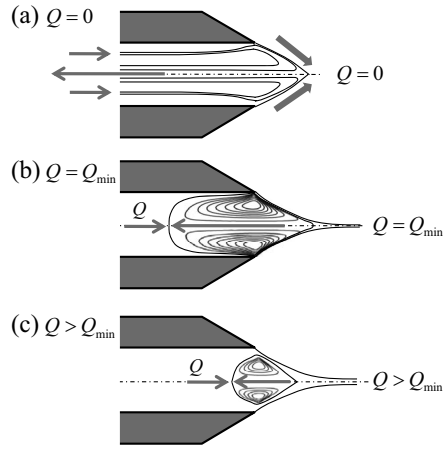
FIG. 10. The role of the recirculation cell in three situations. (a) $Q=0$. Theoretical situation where the recirculation cell would get completely into the tube. The momentum injected through the free surface by the external gas stream would be smaller than that consumed by viscosity in the liquid bulk and the tube wall. This situation is not achieved in practice because the recirculation cell starts and stops intermittently (unsteady dripping). (b) $Q=Q_{min}$. The liquid flow rate pushes the recirculation cell downstream. The cell size is such that the source of momentum just balances the viscous sink. (c) $Q>Q_{min}$. The recirculation cell is pushed further downstream, so that it shrinks or even disappears. The meniscus can be globally stable.

than the radius R_1 of the feeding tube. Otherwise, the cell would get into the feeding tube, the inner wall of the tube would act as a very effective momentum sink, the cell motion would be slowed down, the flow would stall for lack of momentum, and consequently the system would reach an unstable state.

Therefore, $S_r < k_c R_1$, k_c being of order unity, may constitute a necessary condition to reach steady jetting in FF. From Eq. (23), one concludes that the flow rate Q must be greater than

$$Q_{min} = C\frac{D\mu}{\rho} = CQ_D, \qquad (24)$$

where $C=(C_1-k_c)R_1/(C_2 D)$. Let us now introduce the Reynolds number,

$$\mathrm{Re}_S = Q_D/Q_\mu = \frac{\rho D(\Delta P/\rho)^{1/2}}{\mu}, \qquad (25)$$

defined with the maximum attainable velocity at the free surface, $(\Delta P/\rho)^{1/2}$. In general, $C=Q_{min}/Q_D$ depends on Re_S. As $\mathrm{Re}_S \to \infty$, k_c and C reach asymptotically constant values of order unity that depend on the geometry only. In particular, Q_{min}/Q_D does not depend on the pressure drop ΔP in that limit. Figure 10 illustrates the instability mechanism associated with the recirculation cell.

Figure 11 shows the values of Re_D and Re_S measured in the steady jetting regime. The line corresponds to the minimum flow rate Q_{min}/Q_D associated with the recirculation cell. Much care was taken in the experiments for flow rates close to that curve, as explained in the experimental section
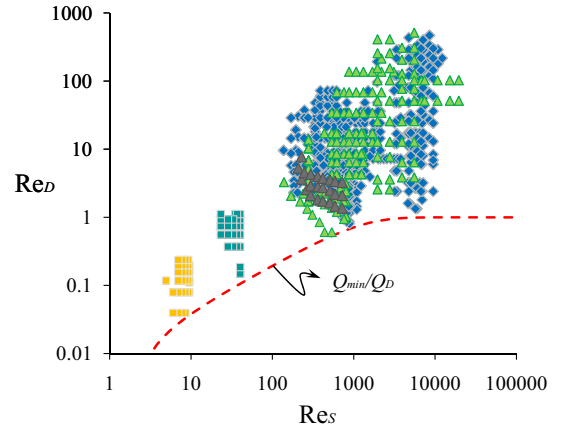

FIG. 11. (Color online) Re_D as a function of Re_S for FF. The symbols are those of Fig. 3. The line is the flow rate Q_{min}/Q_D for which the global instability of the meniscus is reached.

in [43]. As Re_S increases, Q_{min}/Q_D tends to a constant of order unity, as predicted. The line also shows that the minimum flow rate decreases as viscosity increases while keeping the rest of the parameters constant, which indicates that the liquid meniscus is stabilized by the viscosity.

Regarding how momentum is transferred across the meniscus free surface, in ES the momentum transfer is much more pronounced near the apex because the electric field is proportional to the square root of the local mean curvature of the meniscus surface. The influence of the recirculation cell is however less important, and thus the instability mechanism described above for FF is not expected to be relevant in ES.

In summary, we have analyzed in Secs. III and IV the mechanisms setting limiting values to the operational parameters in both ES and FF. The limiting values of the jet parameters We and Ca virtually coincide in ES and FF, a fact which shows that the same physics applies to the instability mechanisms in both cases. An analysis of the limiting mechanisms related to the meniscus yields significant differences between ES and FF, in accord with the different natures of the underlying equilibria in both systems.

V. DROPLET SIZE

The droplet size is finally analyzed in this section for both FF and ES. Figure 12 shows the values of the mass median droplet radius R_d for FF measured when the spray has reached a state with steady droplet size distribution [60]. The droplets are commensurate with the jet diameter due to the Rayleigh instability [9,10]. Therefore, R_d must be on the order of the jet radius R calculated from Eq. (5). As observed in Fig. 12, R_d/R is of order unity for all Weber numbers. The ratio R_d/R depends slightly on We for We $\lesssim 20$, while it decreases significantly as We increases for We $\gtrsim 20$. This is consistent with the spatial stability analysis in [17], where it was found that the most probable breakup wavelength decreases as We increases [17,45]. This behavior has also been observed experimentally [39] and more recently in numerical simulations [43]. In addition, the jet breakup may be gov-
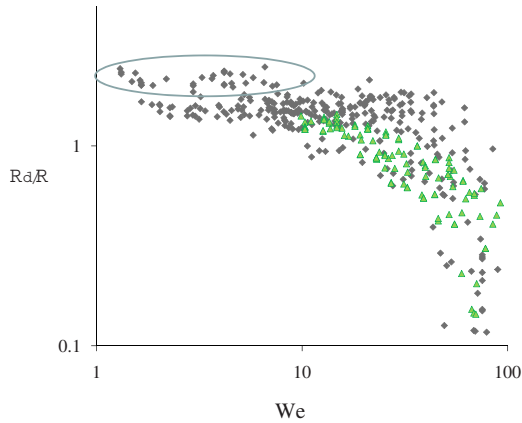
FIG. 12. (Color online) Dimensionless droplet size R_d/R as a function of We for water (diamonds) and ethanol (triangles) nebulized with FF.

erned by the growth of nonaxisymmetric perturbations for We $\gtrsim$ 20 [10]. The scattering of the data for We $\gtrsim$ 10 is far greater for water than for ethanol droplets, probably because of their very different tendencies to coalesce on collision (see, e.g., [61] and references therein). The sharp increase in the scattering of the data for We $\gtrsim$ 20 has been discussed previously [45].

The set of data circled in Fig. 12 lies above the general trend. These data were not reported in [45] because of their plausible correspondence with metastable regimes. Careful observations of the meniscus behavior performed in this work ruled out that explanation. Numerical simulations [43] for We $\lesssim$ 3 have shown that the jet length (relative to its diameter) decreases as the flow rate decreases until the dripping regime is reached. Close to this regime, the droplets tend to coalesce very shortly after the jet breakup. Consequently, close to the dripping regime the average droplet size is larger than that predicted by the Rayleigh breakup. An illustrative movie with a rich sequence is shown in the auxiliary documentation [62]. The movie is extracted from the numerical simulation presented by Herrada *et al.* in Fig. 9(d) of [43]. Although we cannot as yet provide a clear explanation for the set of circled data with We $\gtrsim$ 3, this discrepancy with respect to Rayleigh's prediction might be attributed to enhanced coalescence.

The droplet size for ES is analyzed in Figs. 13 and 14. The ES results for R_d/R are superimposed on those of FF (Fig. 12). Both ES and FF verify similarity law (17) within the interval $1 \lesssim$ We $\lesssim$ 20. We=1 corresponds to the stability limit $Q \simeq Q_\sigma$, while for We $\gtrsim$ 20 there is a significant influence of the Weber number on the axisymmetric breakup wavelength [17] or the jet breakup may be governed by the growth of nonaxisymmetric perturbations [10]. Figure 14 shows the results for the dimensionless droplet size R_d/R_σ, introduced in [63] and extensively used in the literature (see, e.g., [27,31,36,37,47,58] among many others). The solid line R_d/R_σ=We is the scaling law consistent with Eq. (5), while the dashed line R_d/R_σ=We$^{2/3}$ is that defended by de la Mora [6]. The departure of the data from this latter scaling, already indicated by Gamero-Castaño and Hruby [29], is evident.

The analytical results of Higuera (see Eq. (3.7) in [27]) also agree with the experiments in Fig. 14 and scaling (5). The FF data are also plotted as background, showing remarkable agreement with the ES results.

The experimental results shown in Figs. 13 and 14 provide strong support for scaling law (5) for the droplet size in ES. Three important features of that law are the following:

(i) There is no significant influence of the liquid permittivity on the droplet size. This result disagrees with the scaling law proposed in [6,8]. The etiology of this disagreement may require a deeper analysis out of the scope of this paper. The following reflections may serve as a motif for further studies. If one assumes that the order of magnitude of the liquid conductivity is not modified along the jet (in spite of the arguable discussions in [6]), then the available energy to acquire kinetic energy should be on the order of $\sigma K R^2/\varepsilon_0$ [see Eq. (14)]. No more energy can be extracted from the system [29] if the jet length is smaller than the meniscus size, and this leads to a scaling of R and R_d with We. However, for moderately high conductivity liquids for which the jet is sufficiently small to be entirely under the electrical influence of the meniscus, the scaling of de la Mora [6,8] as $R \sim$ We$^{2/3}$ < We implies that the jet would generally extract an energy from some unknown source (other than the electrified meniscus) such that its kinetic energy eventually becomes on the order of $\rho Q K G(\varepsilon)/(\sigma \varepsilon_0)$ times larger than $\sigma K R^2/\varepsilon_0$, where $G(\varepsilon)$ is an *ad hoc* function of the ratio ε between the liquid and vacuum permittivities. Interestingly, the number $\rho Q K G(\varepsilon)/(\sigma \varepsilon_0)$ is generally on the order of 10–10^5 in the experiments.

(ii) Charge relaxation considerations seem unimportant for the scaling of the jet and droplet sizes. This result is supported by the remarkable agreement between the proposed scaling laws and the experimental measurements gathered from the literature. Therefore, the equilibrium electrical conductivity seems not be significantly altered in the whole liquid domain. It is worth noting that, even in those extreme cases where this was not strictly true somewhere along the cone-jet domain [6], the order of magnitude of K could not change in the STS regime according to what the experiments reveal. In fact, the potential existence of charge rarefaction fronts affecting the entire liquid cross section in those extreme cases mentioned would necessarily invoke propagating waves and strongly unsteady processes not generally applicable in STS Taylor cone jets. In this sense, the early ideas proposed in [8] appear to be inconsistent with the discussions provided in [6] by the same author. This may explain the deviations of the experimental measurements from the early scaling laws in [8] and the necessary *ad hoc* adjustments on the liquid polarity dependence to fit the experiments (see Figs. 10–12 in [8]). Those adjustments and the subsequent introduction of the charge rarefaction front phenomena would not be necessary in the STS regime if the liquid polarity was simply left out in the first order analysis and the corresponding scaling laws, as proposed in [7,31,37,64].

(iii) Despite viscous dissipation was neglected in the energy balance, the scaling law agrees reasonably well with the measurements even for relatively large Ca values. We attribute the success of Eq. (14) to the continued stretching that the electric field exerts on the jet, which provides the jet with
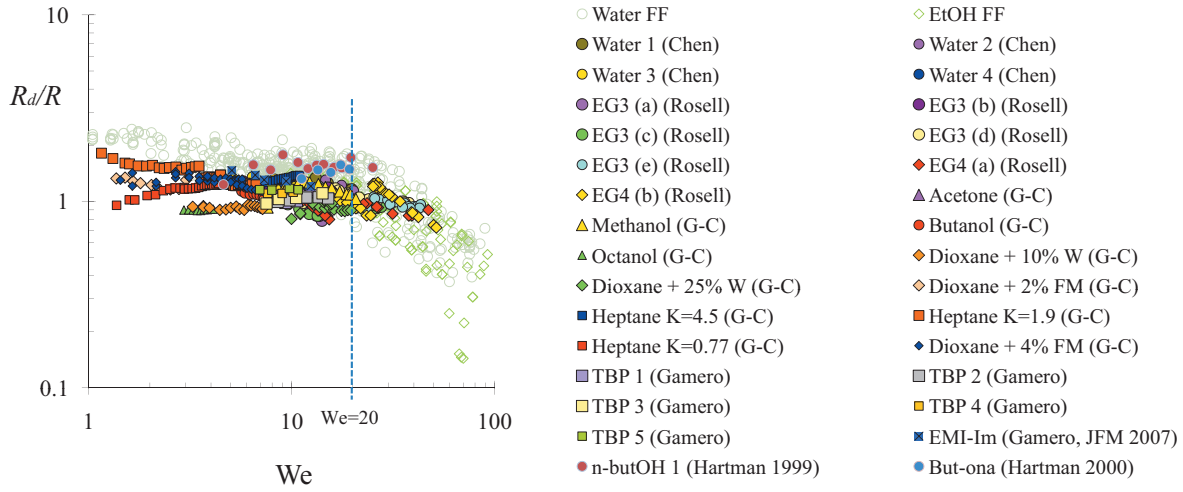
FIG. 13. (Color) Dimensionless droplet size R_d/R as a function of We for both FF and ES. The vertical line is the limit We=20 above which the similarity is lost.

a *final* kinetic energy similar to that of less viscous liquids. When viscous forces become important, the growth rate of the perturbations decreases significantly, and one obtains very long and thinned jets. Interestingly, this thinning leads to diameters corresponding to low viscosity liquids, which acquire their final kinetic energy at shorter distances from the tip. According to scaling (14), this final kinetic energy is dictated by the liquid properties exclusively. It is particularly attractive that the physical symmetries invoked in the conservation of energy seem to extend quite beyond the limits of our hypotheses.

VI. CONCLUSIONS

Both FF and ES working in their most extensively used regime produce high quality sprays composed by homogeneous and well-controlled size droplets. FF and ES utilize locally available differences of energies to produce a steady capillary jet. In both cases, the liquid forms a cusplike meniscus from whose tip tapers a steady jet. The tapering meniscus may be globally stable or unstable depending on the values of the operational parameters. The global stability of the liquid meniscus is a prerequisite for steady jetting. Three factors responsible for global instability were identified in the present study: (i) the energy consumed in the formation of the jet free surface and in the generation of its kinetic energy, (ii) the tangential surface stresses exerted by the focusing coflowing stream in FF to form and sustain a steady tapering meniscus, and (iii) the interaction between the recirculation cell in the meniscus of FF and the feeding tube wall. The first mechanism is associated with the local flow structure in the tip, while the second and third ones are related to the global behavior of the meniscus.

The fluidic structures in the tip of both ES and FF are similar. For low and moderately high viscosity liquids, the scaling law for the jet radius can be obtained from the energy balance taking place in that region of the flow. In this case,
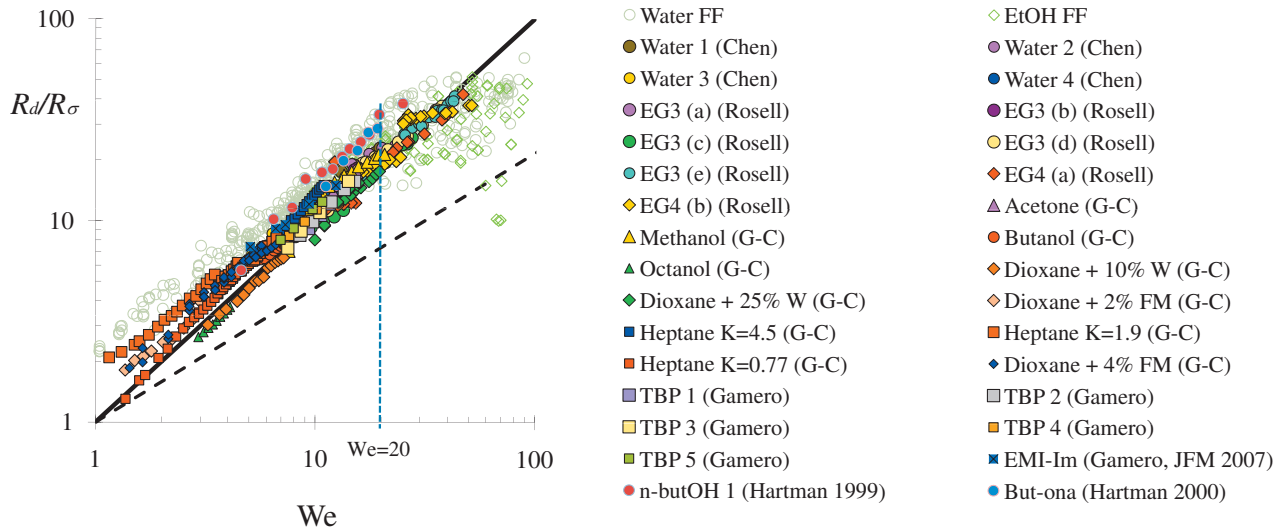

FIG. 14. (Color) Dimensionless droplet size R_d/R_σ as a function of We for both FF and ES. The solid and dashed lines are the functions $R_d/R_\sigma = $ We and $R_d/R_\sigma = $ We$^{2/3}$, respectively. The vertical line is the limit We=20.

the same scaling laws are derived for ES and FF. Because the resulting droplets are commensurate to the jet radius [9,10], the same scaling laws also apply to predict the size of the droplets produced by both atomization techniques. We have found that if the ES results are expressed in terms of effective pressure drop (16), the two phenomena verify the same scaling laws (and stability limits). Effective pressure drop (16) is a function of the liquid properties exclusively, i.e., it does not depend on the operational parameters (flow rate and applied voltage). Experiments conducted in this work and those taken from the literature demonstrated the validity of the proposed scaling law. Specifically, it was shown that the dimensionless droplet radius R_d/R_σ scales as We [7,29,31,37] instead of We$^{2/3}$ [6].

The experimental data also showed that the analogies found between ES and FF are not preserved when considering the instability caused by the meniscus. The differences between the flow structure in the liquid meniscus and the nature of the equilibria of ES and FF yield significant discrepancies between the corresponding stability limits. The comparison of the tangential stresses that the external fields cause on the liquid meniscus revealed a fundamental difference between the jetting phenomenon in ES and FF. Interestingly, the experiments show that while the tangential viscous stress is always larger than the normal surface tension one in FF, the contrary occurs in ES. This disjunction may explain why a peak-ended static solution has not yet been obtained for FF, while ES comfortably sits on Taylor's solution to eject a thin liquid jet.

[1] R. Suryo and O. A. Basaran, Phys. Fluids **18**, 082102 (2006).

[2] R. T. Collins, J. J. Jones, M. T. Harris, and O. A. Basaran, Nat. Phys. **4**, 149 (2008).

[3] L. Oddershede and S. R. Nagel, Phys. Rev. Lett. **85**, 1234 (2000).

[4] S. I. Betelú, M. A. Fontelos, U. Kindelán, and O. Vantzos, Phys. Fluids **18**, 051706 (2006).

[5] J. Fernández de la Mora, J. Colloid Interface Sci. **178**, 209 (1996).

[6] J. Fernández de la Mora, Annu. Rev. Fluid Mech. **39**, 217 (2007).

[7] A. M. Gañán-Calvo, J. Fluid Mech. **507**, 203 (2004).

[8] J. F. de la Mora and I. G. Loscertales, J. Fluid Mech. **260**, 155 (1994).

[9] J. W. S. Rayleigh, *The Theory of Sound* (Cambridge University Press, Cambridge, 1967).

[10] J. M. Gordillo, M. Pérez-Saborid, and A. M. Gañán-Calvo, J. Fluid Mech. **448**, 23 (2001).

[11] P. Huerre and P. A. Monkewitz, Annu. Rev. Fluid Mech. **22**, 473 (1990).

[12] A. M. Gañán-Calvo and P. Riesco-Chueca, J. Fluid Mech. **553**, 75 (2006).

[13] P. Guillot, A. Colin, A. S. Utada, and A. Ajdari, Phys. Rev. Lett. **99**, 104502 (2007).

[14] J. M. Montanero and A. M. Gañán-Calvo, Phys. Rev. E **77**, 046301 (2008).

[15] The growth rate of the most unstable temporal mode is always greater than that corresponding to the absolutely unstable mode [11].

[16] A. M. Gañán-Calvo and J. M. Gordillo, Phys. Rev. Lett. **87**, 274501 (2001).

[17] J. M. Gordillo, A. M. Gañán-Calvo, and M. Pérez-Saborid, Phys. Fluids **13**, 3839 (2001).

[18] M. A. Herrada and A. M. Gañán-Calvo, Phys. Fluids **21**, 042003 (2009).

[19] A. S. Utada, A. Fernández-Nieves, J. M. Gordillo, and D. A. Weitz, Phys. Rev. Lett. **100**, 014502 (2008).

[20] I. Marginean, P. Nemes, and A. Vertes, Phys. Rev. E **76**, 026320 (2007).

[21] A. Jaworek and A. Krupa, J. Aerosol Sci. **30**, 873 (1999).

[22] J. Zeleny, Phys. Rev. **10**, 1 (1917).

[23] I. Hayati, A. I. Bailey, and Th. F. Tadros, J. Colloid Interface Sci. **117**, 205 (1987).

[24] M. Cloupeau and B. Prunet-Foch, J. Electrost. **22**, 135 (1989).

[25] J. Rosell-Llompart and J. Fernández de la Mora, J. Aerosol Sci. **25**, 1093 (1994).

[26] R. P. A. Hartman, D. J. Brunner, D. M. A. Camelot, J. C. M. Marijnissen, and B. Scarlett, J. Aerosol Sci. **30**, 823 (1999).

[27] F. Higuera, J. Fluid Mech. **484**, 303 (2003).

[28] J. Fernández de la Mora, J. Fluid Mech. **243**, 561 (1992).

[29] M. Gamero-Castaño and V. Hruby, J. Fluid Mech. **459**, 245 (2002).

[30] D. R. Chen, D. Y. H. Pui, and S. L. Kaufman, J. Aerosol Sci. **26**, 963 (1995).

[31] A. M. Gañán-Calvo, J. Aerosol Sci. **30**, 863 (1999).

[32] G. I. Taylor, Proc. R. Soc. London, Ser. A **280**, 383 (1964).

[33] C. Pantano, A. M. Gañán-Calvo, and A. Barrero, J. Aerosol Sci. **25**, 1065 (1994).

[34] W. W. Zhang, Phys. Rev. Lett. **93**, 184502 (2004).

[35] J. Eggers (private communication).

[36] J. M. López-Herrera, A. Barrero, A. Boucard, I. G. Loscertales, and M. Marquez, J. Am. Soc. Mass Spectrom. **15**, 253 (2004).

[37] A. M. Gañán-Calvo, Phys. Rev. Lett. **79**, 217 (1997).

[38] A. M. Gañán-Calvo, R. González-Prieto, P. Riesco-Chueca, M. A. Herrada, and M. Flores-Mosquera, Nat. Phys. **3**, 737 (2007).

[39] A. M. Gañán-Calvo, Phys. Rev. Lett. **80**, 285 (1998).

[40] A. M. Gañán-Calvo and J. M. López-Herrera, J. Fluid Mech. **566**, 421 (2006).

[41] D. A. Grigoriev and M. J. Edirisinghe, J. Appl. Phys. **91**, 437 (2002).

[42] This comparison is legitimate since both ΔP and τ_s are applied on surfaces whose projection in the axial direction is comparable to D^2. More specifically, $\int_S \mathbf{n} \cdot \mathbf{e}_z ds \sim O(D^2)$, where $\mathbf{n}$ and $\mathbf{e}_z$ are the normal and axial unitary vectors, respectively, and S is the meniscus surface.

[43] M. A. Herrada, A. M. Gañán-Calvo, A. Ojeda-Monge, B. Bluth, and P. Riesco-Chueca, Phys. Rev. E **78**, 036323 (2008).

[44] L. Martín-Banderas, M. Flores-Mosquera, P. Riesco-Chueca, A. Rodríguez-Gil, A. Cebolla, S. Chávez, and A. M. Gañán-Calvo, Small **1**, 688 (2005).

[45] J. Rosell-Llompart and A. M. Gañán-Calvo, Phys. Rev. E **77**, 036321 (2008).

[46] D. A. Saville, Annu. Rev. Fluid Mech. **29**, 27 (1997).

[47] A. M. Gañán-Calvo, J. Dávila, and A. Barrero, J. Aerosol Sci. **28**, 249 (1997).

[48] It was shown in [33] that for each feeding capillary-electrode configuration and for a given meniscus volume, there is a single value of the applied voltage V for which an electrostatic solution exists. When a thin jet is steadily emitted, it breaks up into a fine spray downstream. The voltage drop in the axial direction is limited by the presence of the charged spray. As a consequence, the applied voltage must be slightly increased to maintain the steady jetting.

[49] A. M. Gañán-Calvo, J. Fluid Mech. **335**, 165 (1997).

[50] A. K. Sen, J. Darabi, D. R. Knapp, and J. Liu, J. Micromech. Microeng. **16**, 620 (2006).

[51] J. M. López-Herrera, P. Riesco-Chueca, and A. M. Gañán-Calvo, Phys. Fluids **17**, 034106 (2005).

[52] G. I. Barenblatt, *Scaling* (Cambridge University Press, Cambridge, 2003).

[53] S. J. Leib and M. E. Goldstein, Phys. Fluids **29**, 952 (1986).

[54] A. M. Gañán-Calvo, Phys. Rev. Lett. **98**, 134503 (2007).

[55] A. M. Gañán-Calvo, Phys. Rev. E **78**, 026304 (2008).

[56] M. Gamero-Castaño, Phys. Fluids **20**, 032103 (2008).

[57] M. Gamero-Castaño, J. Fluid Mech. **604**, 339 (2008).

[58] I. Guerrero, R. Bocanegra, F. J. Higuera, and J. F. de la Mora, J. Fluid Mech. **591**, 437 (2007).

[59] In the experiments in Ref. [50], a capillary with an inner sharp microrod of 5 μm in diameter was used to stabilize the liquid meniscus and to favor the liquid anchorage. This geometrical configuration does not correspond to that assumed in the present study. For this reason, we have excluded the data in Fig. 9 of [50].

[60] J. C. Lasheras and E. C. Hopfinger, Annu. Rev. Fluid Mech. **32**, 275 (2000).

[61] J. Qian and C. K. Law, J. Fluid Mech. **331**, 59 (1997).

[62] See EPAPS Document No. E-PLEEE8-79-038906 for an illustrative movie. For more information on EPAPS, see http://www.aip.org/pubservs/epaps.html.

[63] A. M. Gañán-Calvo, J. C. Lasheras, J. Dávila, and A. Barrero, J. Aerosol Sci. **25**, 1121 (1994).

[64] A. M. Gañán-Calvo, A. Barrero, and C. Pantano, J. Aerosol Sci. **24**, S19 (1993).

[65] R. P. A. Hartman, D. J. Brunner, D. M. A. Camelot, J. C. M. Marijnissen, and B. Scarlett, J. Aerosol Sci. **31**, 65 (2000).

[66] D. Garoz, C. Bueno, C. Larriba, S. Castro, I. Romero-Sanz, J. F. De La Mora, Y. Yoshida, and G. Saito, J. Appl. Phys. **102**, 064913 (2007).

[67] L. F. Velásquez-García, A. I. Akinwande, and M. Martínez–Sánchez, J. Microelectromech. Syst. **15**, 1260 (2006).

[68] J. Eggers and E. Villermaux, Rep. Prog. Phys. **71**, 036601 (2008).